Received ; | Revised ; | Accepted

DOI: xxx/xxxx

RESEARCH ARTICLE

A framework for isogeometric-analysis-based design and optimization of wind turbine blade structures

Austin J. Herrema*[1] | Josef Kiendl[2] | Ming-Chen Hsu[1]

[1]Department of Mechanical Engineering, Iowa State University, 2025 Black Engineering, Ames, Iowa 50011, USA

[2]Department of Marine Technology, Norwegian University of Science and Technology, O. Nielsens veg 10, 7052 Trondheim, Norway

Correspondence

*Austin J. Herrema, Department of Mechanical Engineering, Iowa State University, 2025 Black Engineering, Ames, Iowa 50011, USA. Email: austin.j.he@gmail.com

Summary

Typical blade design procedures employ reduced-order models almost exclusively for early-stage design; high-fidelity, finite element-based procedures are reserved for later design stages because of complex workflows and high computational expense. Yet, high-fidelity structural analyses often provide design-governing feedback such as buckling load factors. Addressing the issues of workflow complexity and computational expense would allow designers to utilize this high-fidelity feedback earlier, more easily, and more often in the design process. Thus, a blade analysis framework is presented which employs isogeometric analysis (IGA), a simulation method that overcomes many of the aforementioned drawbacks associated with typical finite element analysis (FEA). IGA directly utilizes the mathematical models generated by computer-aided design (CAD) software, requiring less user interaction and no conversion of parametric geometries to finite element meshes, and tends to have superior per-degree-of-freedom accuracy compared to traditional FEA. Issues unique to IGA in the context of wind turbine blade design, such as coupling of thin-shell components, are addressed, and a design framework that combines reduced-order aeroelastic analysis with IGA is outlined. Aeroelastic analysis is used in the design framework to efficiently provide dynamic kinematic data for a wide range of wind load cases, while IGA is used to perform buckling analysis. The value of incorporating high-fidelity analysis feedback into blade design is demonstrated through optimization of the NREL/SNL 5 MW wind turbine blade. A variety of potential designs are produced with reduced blade mass and material cost, and IGA-based buckling analysis is shown to provide design-governing constraint information.

KEYWORDS:

blade design; optimization; finite element; isogeometric analysis; buckling; NREL/SNL 5 MW

1 | INTRODUCTION

The trend of increasing wind turbine blade length is ultimately driven by the pursuit of lower cost wind energy through larger swept areas. However, under some basic assumptions, it can be shown that while rotor power increase is related to rotor size through a quadratic relationship, rotor weight is related to rotor size through a cubic relationship.[1] This is known as the cube-square law and it suggests significant challenges in the design of larger blades, especially because cost-effectiveness is a priority. Although the cube-square law appears to have been overcome in practice through a variety of design methods,[2] increasing blade length nevertheless entails considerable structural design challenges as a result of shifts in design-governing phenomena. In particular, it has been suggested that blade buckling, especially with regard to nonlinear effects, is of increasing concern.[3–7]

Wind turbine blade design typically relies heavily on computationally efficient, reduced-order aerodynamic and structural models, especially in the early stages of blade design. This is a sensible approach given a vast design space, the large number of design iterations typically performed, and the ample accuracy of many reduced-order models. The value of such an approach can be especially realized in the context of optimization.[8–14] Some types of analyses, however, are more difficult to perform reliably using reduced-order models. Thus, higher-fidelity finite element analysis (FEA), including both shell and solid FEA, is typically employed in the later design stages to evaluate, for example, buckling load factors as required by design standards such as the IEC 61400.[15] Because blades are often optimized without taking this accurate buckling feedback into account, late-stage FEA can reveal design flaws that trigger additional, laborious design iteration. Notably, the focus during these iterations usually shifts away from blade optimality and towards satisfaction of design standards. While an ideal design procedure would incorporate accurate buckling feedback throughout optimization, the computational cost and labor associated with traditional high-fidelity analyses are prohibitive. Improving high-fidelity structural analysis workflows and methodologies could improve not only design iteration that occurs in later blade design stages, but also the feasibility of incorporating accurate high-fidelity analyses into optimization.

The present work therefore outlines a framework for isogeometric analysis (IGA)-based design and optimization of wind turbine blade structures. IGA was first introduced by Hughes et al.[16] and is based on the idea that the smooth, parametric functions used in computer-aided design (CAD) can also be used as finite element basis functions, eliminating the need for extra mesh generation. IGA is therefore capable of effectively uniting design and analysis paradigms, employing a single model for all such activities, and ultimately reducing designer labor and requisite user interaction. IGA has also been shown to feature significantly improved per-degree-of-freedom accuracy relative to traditional FEA in many cases.[17,18] Past wind turbine and wind turbine blade simulations have employed IGA,[19–30] but none of these efforts have simultaneously integrated IGA into a parametric design environment, employed practical, discretization-agnostic methodologies for coupling NURBS surfaces in analysis, and engaged various types of structural analyses, such as buckling analysis, that are particularly relevant in blade design. The present framework addresses each of these issues and is demonstrated through the modeling, analysis, and optimization of the NREL/SNL 5 MW reference blade design.

This paper is outlined as follows. The salient theoretical and technical aspects of the presented framework for isogeometric analysis of wind turbine blades are described in Section 2. In Section 3, the details of the reference 5 MW blade model are described, and the IGA-based model is presented and analyzed. Additionally, a mesh convergence study is performed and compared to results obtained using traditional FEA. In Section 4, the 5 MW blade design is optimized using a combination of reduced-order aeroelastic analyses and IGA-based buckling analysis. Lastly, Section 5 presents a variety of conclusions based on construction and employment of the IGA-based framework for design and optimization of the 5 MW blade.

2 | FRAMEWORK FOR ISOGEOMETRIC ANALYSIS OF WIND TURBINE BLADES

2.1 | Isogeometric analysis fundamentals

Typical FEA methods rely on networks of interpolants to represent a solution field. The network, and hence the analysis space, is generally constructed by generating a finite element mesh consisting of nodes, at which the solution of interest is directly represented, and elements, over which the solution field is represented by specified functions. Geometries in FEA are represented by finite element meshes comprised of, for example, linear triangular elements. Conversely, CAD systems typically employ a variety of analytic or parametric functions, such as splines, for advanced geometry representation, visualization and manipulation. For the engineering designer utilizing both CAD and computer-aided engineering (CAE), these unique geometric paradigms entail the management of separate, but necessarily related, geometry descriptions. This can lead to a significant amount of manual labor for the design engineer.[31]

The core recognition of Hughes et al.[16] was that the parametric functions used by CAD systems to represent geometry can also be used to represent the solution fields of partial differential equations. For example, if an object is modeled geometrically using non-uniform rational B-splines (NURBS), which are employed in this work, the solution field can readily be represented using the exact same set of NURBS functions. In addition to the practical advantages suggested by this approach, such as only needing to maintain a single geometry description throughout design and analysis, NURBS basis functions have a number of properties making them useful for analysis, including partition of unity and non-negativity.[16]

Because they are central to geometry modeling, the structural analysis performed in this work, and to NURBS-based IGA in general, the mathematical background of NURBS functions, which are a generalization of B-splines, is given here. Given a parametric variable u, a B-spline curve is defined by a set of non-interpolated control points, $\mathbf{P}_i, i = 1, \ldots, n$; degree, p; and a knot vector, $U = [u_1, u_2, \ldots, u_{n+p+1}]$, which is a set of parametric coordinates dividing the curve into segments over which distinct sets of basis functions have influence. The basis functions are defined by the

Cox-deBoor recursion formula.[32] For degree $p = 0$,

$$N_{i,0}(u) = \begin{cases} 0 & \text{if} \quad u_i \leq u < u_{i+1}\,, \\ 1 & \text{otherwise,} \end{cases} \tag{1}$$

and for degree $p \geq 1$,

$$N_{i,p}(u) = \frac{u - u_i}{u_{i+p} - u_i} N_{i,p-1}(u) + \frac{u_{i+p+1} - u}{u_{i+p+1} - u_{i+1}} N_{i+1,p-1}(u)\,. \tag{2}$$

These B-spline basis functions can be further generalized to define NURBS entities. For each of the n control points, $\mathbf{P}_i$, a weight, w_i, is assigned. These weights are used to describe the relative strength of influence of a basis function, in effect defining new, rational basis functions:

$$R_i^p(u) = \frac{N_{i,p}(u) w_i}{\sum_{j=0}^{n} N_{j,p}(u) w_j}\,. \tag{3}$$

A NURBS curve can therefore be defined as a linear combination of the n basis functions and n control points:

$$\mathbf{C}(u) = \sum_{i=0}^{n} R_i^p(u) \mathbf{P}_i\,. \tag{4}$$

For a net of $m \times n$ control points, $\mathbf{P}_{i,j}$, and weights, $w_{i,j}$, and with the introduction of a second parametric direction, v; associated knot vector, V; degree, q; and set of basis functions, $N_{j,q}(v)$; a similar approach can be used to define bi-directional rational basis functions and NURBS surfaces:

$$R_{i,j}^{p,q}(u,v) = \frac{N_{i,p}(u) N_{j,q}(v) w_{i,j}}{\sum_{k=0}^{n} \sum_{l=0}^{m} N_{k,p}(u) N_{l,q}(v) w_{k,l}}\,, \tag{5}$$

$$\mathbf{S}(u,v) = \sum_{i=0}^{n} \sum_{j=0}^{m} R_{i,j}^{p,q}(u,v) \mathbf{P}_{i,j}\,. \tag{6}$$

If $w_{i,j} = 1$ for all i and j, then $\mathbf{S}(u,v)$ becomes a B-spline surface. Much of the utility of both surface modeling and IGA is owed to the advantageous characteristics of these functions; more of the mathematical details of NURBS are given by Piegl and Tiller[32] and Hughes et al.[16] IGA relies on the utilization of such functions to derive appropriate variational formulations for partial differential equations. For NURBS-based structural analyses, the degrees of freedom are usually defined as the displacement of the control points.

As is the case in traditional FEA, the concept of "elements" is employed in IGA. In NURBS-based IGA, the spaces in between the knots in a valid knot vector are considered elements. For example, given a knot vector of $U = [0, 0, 0, 1, 2, 3, 3, 3]$, the parametric space $u = [0, 1]$ is considered an element. This definition is employed despite the fact that some of basis functions that are active in the space of this element remain active beyond $u = 1$, a key distinction from traditional finite elements. As in traditional FEA, mesh refinement is an important procedure in IGA, with both h-refinement, which corresponds to *knot insertion* of NURBS functions, and p-refinement, which corresponds to *degree elevation*, possible. Utilizing p-refinement entails changing the degree of the functions being used (e.g. NURBS), whereas h-refinement inserts knots to "divide" elements. k-refinement, which consists of p-refinement followed by h-refinement, is also possible in IGA and has some beneficial qualities. For more information, details about both IGA and the use of NURBS in the context of IGA are described by Hughes et al.[16]

2.2 | Isogeometric analysis of thin-shell composites

Wind turbine blades are commonly analyzed as shell structures. An isogeometric Kirchhoff–Love thin-shell formulation was first proposed by Kiendl et al.[33] and was reformulated for composite shells by Bazilevs et al.[20] The thin-shell formulation was shown by Korobenko et al.[24] to accurately model wind turbine blade kinematics and is computationally advantageous relative to thick-shell formulations in that it does not feature rotational degrees of freedom. This makes it a particularly appropriate formulation for the purposes of iterative design.

The structural formulation is as based on the virtual work expression

$$\int_{\mathcal{S}} \delta\boldsymbol{\varepsilon} \cdot (\mathbf{A}\boldsymbol{\varepsilon} + \mathbf{B}\boldsymbol{\kappa})\, \mathrm{d}\mathcal{S} + \int_{\mathcal{S}} \delta\boldsymbol{\kappa} \cdot (\mathbf{B}\boldsymbol{\varepsilon} + \mathbf{D}\boldsymbol{\kappa})\, \mathrm{d}\mathcal{S} = \int_{\mathcal{S}} \delta\mathbf{u} \cdot \mathbf{f}\, \mathrm{d}\mathcal{S}\,, \tag{7}$$

where $\mathcal{S}$ denotes the shell midsurface in the reference configuration; $\mathbf{A}$, $\mathbf{B}$, and $\mathbf{D}$ are the extensional (membrane), coupling, and bending stiffnesses, respectively, written with respect to the local Cartesian basis[1] and calculated using classical laminated plate theory[34]; $\boldsymbol{\varepsilon}$ and $\boldsymbol{\kappa}$ are the membrane strain and curvature change of the midsurface, respectively; and $\delta\varepsilon$ and $\delta\boldsymbol{\kappa}$ are their virtual counterparts corresponding to a virtual displacement $\delta\mathbf{u}$. The load vector $\mathbf{f}$ represents both distributed external loads as well as (thickness-integrated) body loads.

[1] In this work, the local Cartesian basis is oriented on the first covariant base vector of the midsurface, which is aligned with the first parametric direction of the NURBS surface.

Because second order derivatives appear in the governing variational equations of the Kirchhoff–Love theory, C^1-continuous approximation functions are required. This implies that traditional low-order finite element approaches cannot be readily used to perform thin-shell analysis, usually leading to the introduction of rotational degrees of freedom. In contrast, CAD-based functions, such as NURBS, are naturally C^1-continuous and can be directly employed for thin-shell analysis.

2.3 | Coupling of surface patches with matching or non-matching discretization

Despite the advantages offered by the isogeometric Kirchhoff–Love approach, maintaining C^1 continuity of the approximation functions throughout the entirety of a given structure is often unfeasible. As a result of the underlying CAD technology, designer intent, or some combination thereof, models of complex, real-world objects are often composed of many NURBS surface patches. This indicates only C^0 or even C^{-1} continuity between patches, the latter meaning that small gaps or overlaps between adjacent patches might appear. Such situations naturally occur in the modeling of, for example, wind turbine blades because the outer shell of the blade and its shear webs cannot be modeled using a single NURBS patch.

A variety of approaches for coupling thin-shell components have been offered in the field of IGA.[35–41] One of the most well-known methods is the bending strip method, first introduced by Kiendl et al.[42] The method introduces NURBS-based strips of fictitious material featuring unidirectional bending stiffness and zero membrane stiffness and was shown in multiple instances[20,25,42] to be effective in performing IGA-based simulation of wind turbine blade structures that were modeled using multiple NURBS patches. A key drawback of the bending strip method, however, is that it requires the NURBS control points on the two patches that are to be coupled to be coincident at the coupling location, also known as conforming discretization. This is difficult to achieve in some circumstances and greatly constrains the geometry construction procedure.

A coupling approach that is capable of coupling non-matching interfaces by imposing both displacement and rotational continuity via penalty formulations was proposed by Breitenberger et al.[39] However, their formulation for rotational continuity was restricted to rotation angles less than $\pi/2$. Duong et al.[41] have presented a different penalty formulation for the rotational continuity which has no limitation on the rotational angle but which is only applied to conforming patches. In the present paper, the approach presented by Duong et al.[41] is extended to non-matching patches in order to maximize the flexibility of the coupling methodology.

Considering a patch interface between two surface patches $\mathcal{S}^{\mathsf{A}}$ and $\mathcal{S}^{\mathsf{B}}$, such as the patches used to model the spar cap and shear web in Figure 1, two separate penalty energies for undesirable jumps in displacements and rotations are defined. The displacement penalty energy W^{pd} is obtained in a standard form as

$$\mathsf{W}^{\mathsf{pd}} = \alpha_{\mathsf{d}} \int_{\mathcal{L}^{\mathsf{AB}}} \left(\mathbf{u}^{\mathsf{A}} - \mathbf{u}^{\mathsf{B}}\right)^2 \mathrm{d}\mathcal{L}\,, \tag{8}$$

where $\mathcal{L}^{\mathsf{AB}}$ denotes the patch interface, $\mathbf{u}^{\mathsf{A}}$ and $\mathbf{u}^{\mathsf{B}}$ are the displacements of the corresponding points on surface patches $\mathcal{S}^{\mathsf{A}}$ and $\mathcal{S}^{\mathsf{B}}$, respectively, and α_{d} is a penalty parameter of large magnitude. For the rotational continuity between the two surfaces, the rotational penalty energy[41] is defined as

$$\mathsf{W}^{\mathsf{pr}} = \alpha_{\mathsf{r}} \int_{\mathcal{L}^{\mathsf{AB}}} \left((\cos\phi - \cos\phi_0)^2 + (\sin\phi - \sin\phi_0)^2\right) \mathrm{d}\mathcal{L}\,, \tag{9}$$

where ϕ_0 and ϕ are the angles between the surfaces before and after deformation, respectively. The virtual work formulation, Equation 7, is augmented by the variations of W^{pd} and W^{pr} and restated as

$$\int_{\mathcal{S}} \delta\boldsymbol{\varepsilon} \cdot (\mathbf{A}\boldsymbol{\varepsilon} + \mathbf{B}\boldsymbol{\kappa})\, \mathrm{d}\mathcal{S} + \int_{\mathcal{S}} \delta\boldsymbol{\kappa} \cdot (\mathbf{B}\boldsymbol{\varepsilon} + \mathbf{D}\boldsymbol{\kappa})\, \mathrm{d}\mathcal{S} + \delta\mathsf{W}^{\mathsf{pd}} + \delta\mathsf{W}^{\mathsf{pr}} = \int_{\mathcal{S}} \delta\mathbf{u} \cdot \mathbf{f}\, \mathrm{d}\mathcal{S}\,. \tag{10}$$

For more details on the variations of the penalty energies, the reader is referred to Duong et al.[41]

In the present framework the two penalty parameters α_{d} and α_{r} are linked to a single dimensionless parameter, α, as follows:

$$\alpha_{\mathsf{d}} = \alpha \frac{\min(\max_{\mathsf{i},\mathsf{j}}(\mathsf{A}^{\mathsf{A}}_{\mathsf{ij}}), \max_{\mathsf{i},\mathsf{j}}(\mathsf{A}^{\mathsf{B}}_{\mathsf{ij}}))}{(\mathsf{h}^{\mathsf{A}} + \mathsf{h}^{\mathsf{B}})/2} \qquad \mathsf{i} = 1,2, \qquad \mathsf{j} = 1,2\,, \tag{11}$$

$$\alpha_{\mathsf{r}} = \alpha \frac{\min(\max_{\mathsf{i},\mathsf{j}}(\mathsf{D}^{\mathsf{A}}_{\mathsf{ij}}), \max_{\mathsf{i},\mathsf{j}}(\mathsf{D}^{\mathsf{B}}_{\mathsf{ij}}))}{(\mathsf{h}^{\mathsf{A}} + \mathsf{h}^{\mathsf{B}})/2} \qquad \mathsf{i} = 1,2, \qquad \mathsf{j} = 1,2\,, \tag{12}$$

where $\mathsf{A}^{\mathsf{A}}_{\mathsf{ij}}$ and $\mathsf{A}^{\mathsf{B}}_{\mathsf{ij}}$ are the elements of local extensional stiffness matrices on surfaces $\mathcal{S}^{\mathsf{A}}$ and $\mathcal{S}^{\mathsf{B}}$ determined using classical laminated plate theory,[34] $\mathsf{D}^{\mathsf{A}}_{\mathsf{ij}}$ and $\mathsf{D}^{\mathsf{B}}_{\mathsf{ij}}$ are the elements of local bending stiffness matrices, and h^{A} and h^{B} are the length of the local elements in the direction most parallel to the penalty curve $\mathcal{L}^{\mathsf{AB}}$. This formulation, along with an overall penalty parameter of $\alpha = 10^3$, works effectively for a wide range of blade analyses, reducing the extent to which the penalty-based approach is problem-dependent.

The interface curve $\mathcal{L}^{\mathsf{AB}}$ is a NURBS curve that can be easily generated for arbitrary configurations in most CAD systems. When performing numerical integration of Equations 8 and 9, the integrands must be evaluated at quadrature points along $\mathcal{L}^{\mathsf{AB}}$ which requires information from

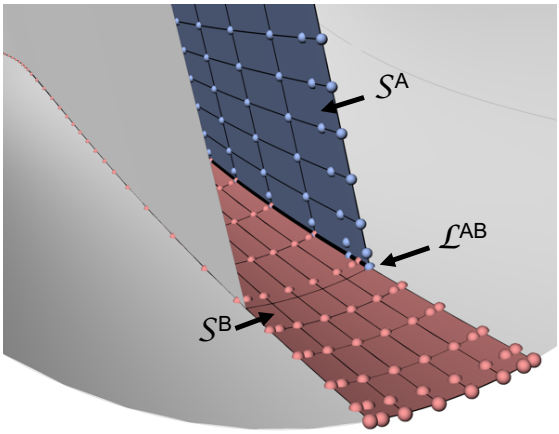

FIGURE 1 Two NURBS surfaces, $\mathcal{S}^{\mathrm{A}}$ and $\mathcal{S}^{\mathrm{B}}$, representing the spar cap and shear web of a wind turbine blade and which must be coupled along the curve $\mathcal{L}^{\mathrm{AB}}$. Control point locations indicated by spheres.

both surfaces $\mathcal{S}^{\mathrm{A}}$ and $\mathcal{S}^{\mathrm{B}}$. For configurations in which a mapping between the parametric spaces of $\mathcal{L}^{\mathrm{AB}}$, $\mathcal{S}^{\mathrm{A}}$, and $\mathcal{S}^{\mathrm{B}}$ can be easily determined, this evaluation is straightforward. For more complex configurations, especially when $\mathcal{L}^{\mathrm{AB}}$ is an approximation of the intersection of surfaces $\mathcal{S}^{\mathrm{A}}$ and $\mathcal{S}^{\mathrm{B}}$, this information is obtained from the points on $\mathcal{S}^{\mathrm{A}}$ and $\mathcal{S}^{\mathrm{B}}$ nearest to a given quadrature point on $\mathcal{L}^{\mathrm{AB}}$.

2.4 | Parametric generation of blade geometry

Reliable, parametric generation of NURBS geometries is a nontrivial task. Given a wind turbine blade's planform and material properties, it is critical to employ a set of geometric operations that will generate a model to which Equation 10 can be applied. And, for the purposes of design, this set of operations should be applicable across a range of design parameters. Following the work presented by Herrema et al.,[29] the CAD software Rhinoceros 3D, a purely NURBS-based platform, and Grasshopper 3D, a visual programming interface for Rhinoceros, are employed. The programmatic approach of Grasshopper allows consistent generation of geometries for a range of parametric inputs whereas its interactive nature enables efficient, intuitive alteration of the underlying algorithms used to generate geometries. The algorithm used to generate the wind turbine blade geometry featured in this work is fundamentally the same as that presented by Herrema et al.[29] but with enhancements to facilitate generation of shear web geometries, division of the high- and low-pressure surfaces into distinct material zones, and flatback airfoils. While a single geometry is used in this work, this approach could be used to generate a wide range of blade geometries.

2.5 | Implementation

A variety of types of analysis, such as deflection, buckling, and vibration analysis, are typically performed throughout wind turbine blade design. The presented framework for IGA-based blade design has been intentionally developed with such flexibility in mind. Specifically, the Fortran-based IGA code employs the Portable, Extensible Toolkit for Scientific Computation (PETSc),[43,44] a suite of data structures and routines intended to enable efficient solution of a wide range of computational problems. PETSc provides access to numerous methods for solution of linear algebra problems. For example, the use of the penalty method, as specified in Equation 10, can produce ill-conditioned stiffness matrices, suggesting use of one of the direct solvers available in PETSc. Additionally, PETSc provides a convenient interface to the Scalable and Flexible Toolkit for the Solution of Eigenvalue Problems (SLEPc),[45,46] allowing relatively straightforward and efficient solution of eigenvalue problems that arise in, for example, vibration analysis (see Section 3.2) and buckling analysis (see Section 3.3). The use of PETSc and SLEPc ensures that the framework can be tuned and adapted to new types of analyses with relative ease and efficiency.

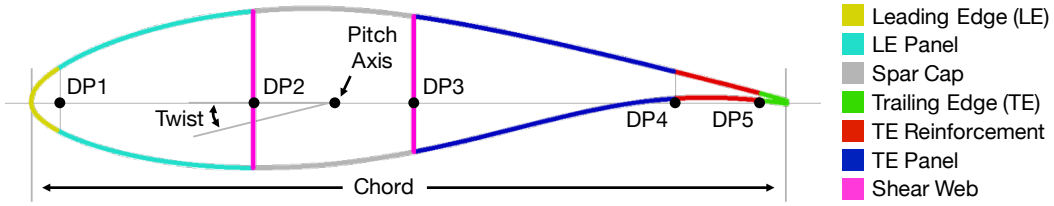

FIGURE 2 Illustration of parameters defined at each station along the blade span in order to define blade geometry and material regions. Parameter values for the NREL/SNL 5 MW blade are given in Table A1.

3 | 5 MW BLADE ANALYSIS

In order to demonstrate the effectiveness of the framework described in Section 2, the NREL/SNL 5 MW reference blade is modeled and analyzed. After defining the reference 5 MW wind turbine blade model in Section 3.1, the model is verified through vibration analysis in Section 3.2. Additionally, because buckling analysis is of particular interest, the linear buckling problem is posed in Section 3.3. Lastly, a mesh refinement study is performed in Section 3.4 which underscores the attractive performance of the IGA-based framework.

3.1 | NREL/SNL 5 MW blade model

The National Renewable Energy Laboratory (NREL) 5 MW blade was first introduced by Jonkman et al.[47] in the context of a full 5 MW turbine definition intended to be a reference for offshore system development. The turbine is a three-bladed, upwind, variable-speed, variable-pitch machine that is loosely representative of modern utility-scale turbines. The geometric definition of the NREL 5 MW blade itself, however, was only intended to support basic aerodynamic analysis and did not contain enough detail to support construction of a three-dimensional CAD model. Further, only the distributed structural properties of the blade are given, rather than a complete composite layup. Resor,[48] as a part of Sandia National Laboratories (SNL), therefore established a rudimentary structural design that approximately reproduces the distributed structural properties described by Jonkman et al.[47] The design also includes a more detailed geometry definition suitable for generation of high quality surface geometries. The wind turbine blade definition described in Resor et al.[48] will hereafter be referred to as the NREL/SNL 5 MW blade.

The properties of each airfoil cross section describing the NREL/SNL 5 MW blade are given in Table A1. In addition to defining the properties needed to establish a baseline aerodynamic profile—such as airfoil type, twist degree, and pitch axis location—the table also describes the location of the material division points needed to divide the blade into distinct material zones. The parameters that are defined at each spanwise station are illustrated in Figure 2.

The parameter values given in Table A1 are used to develop a NURBS-based shell model consisting of multiple NURBS surfaces, each indicating a material zone with a distinct material stacking sequence. The relatively high spanwise resolution of cross sections in Table A1 is not actually required to maintain geometric accuracy. However, the modeling software used by Resor[48] assumes that stacks of materials have constant thickness between stations, indicating that many interpolated stations must be defined to sufficiently represent significant ply drops. In the present work, material thicknesses are defined as piecewise linear functions of blade span which are evaluated at every integration point to determine material distribution. This simplification eliminates the need to use all stations for model construction. More information is given in the footnotes of Table A1. The baseline IGA model is shown in Figure 3 with different colors indicating distinct material zones.

Each of the material zones indicated in Figure 3 employs a unique sequence of material stacks. Each of these material stacks consists of a single orthotropic material with a distinct spanwise thickness distribution as defined in Figure 4. Material properties are described in Table 1 where E_1 and E_2 are the Young's modulus in the first and second material directions, respectively; G_{12} is the shear modulus; ν_{12} is Poisson's ratio; ρ is the density; σ_{UT} is the ultimate tensile strength; and σ_{UC} is the ultimate compressive strength. Further details are given by Resor[48] and Griffith and Ashwill.[49] As Griffith and Ashwill explain, the material properties reported in Table 1 for Saertex and SNL Triax represent the homogenized properties of layups having non-uniform, symmetric fiber orientations. Thus, in the stacking sequences described in Figure 3, these homogenized materials, and all other materials, are assumed to have an overall fiber orientation of zero degrees. In this work, the material axes are aligned with the local Cartesian basis. As a result, the first material direction is aligned with the spanwise parametric direction of the local NURBS surface patch.

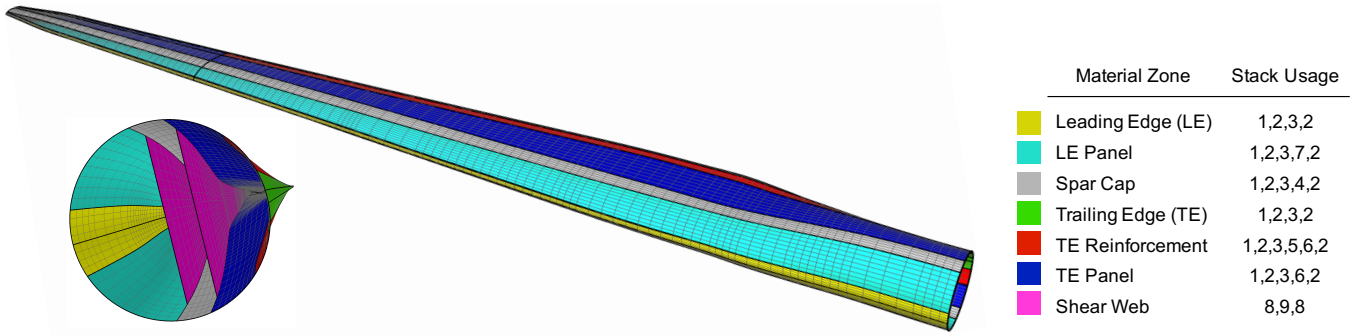

FIGURE 3 A NURBS-based model of the NREL/SNL 5 MW blade. Colors indicate zones with distinct material stacking sequences. Grey lines indicate element edges and black lines indicate surface patch edges. Stacking sequence for each material zone provided; stack definitions can be found in Figure 4.

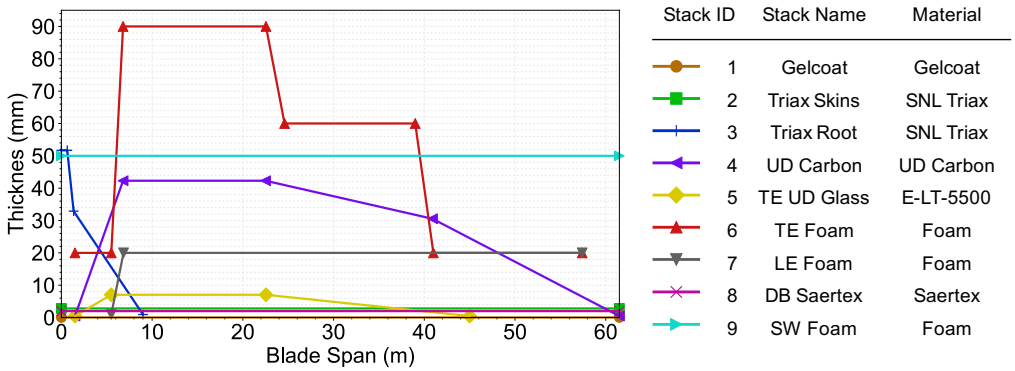

FIGURE 4 Definition of material stack ID, name, material, and spanwise thickness distribution.

TABLE 1 Orthotropic material properties used in the NREL/SNL 5 MW blade design.

Material Name	Layer Thickness (mm)	E_1 (GPa)	E_2 (GPa)	G_{12} (GPa)	ν_{12} (-)	ρ (kg/m^3)	σ_{UT} (GPa)	σ_{UC} (GPa)
Gelcoat	0.05	3.440	3.440	1.323	0.30	1235	-	-
E-LT-5500	0.47	41.80	14.00	2.630	0.28	1920	0.972	0.702
SNL Triax	0.94	27.70	13.65	7.200	0.39	1850	0.700	-
Saertex	1.00	13.60	13.30	11.80	0.49	1780	0.144	0.213
Foam	1.00	0.256	0.256	0.022	0.30	200	-	-
UD Carbon	0.47	114.5	8.390	5.990	0.27	1.220	1.546	1.047

3.2 | Model verification through vibration analysis

Having constructed a model of the NREL/SNL 5 MW blade that is suitable for IGA, a variety of analyses can be performed using the methodology described in Section 2. The vibrational frequencies of a wind turbine blade are important to quantify throughout design in order to avoid resonance phenomena. Because vibration analysis incorporates both the mass properties and the stiffness properties of a structure, it is also a good candidate for comparing the presented IGA-based 5 MW model to the reference[48] model. In the finite element context, linear vibration analysis can be performed by considering the eigenvalue problem

$$\left(\mathbf{K}^{\text{lin}} - \lambda_i \mathbf{M}\right) \mathrm{v}_i = 0\,, \tag{13}$$

where $\mathbf{K}^{\text{lin}}$ is the linear stiffness matrix of the structure, $\mathbf{M}$ is the mass matrix, and λ_i is the i^{th} eigenvalue associated with mode vector v_i. The relation of the i^{th} frequency of vibration, ω_i, to the eigenvalue is given by the equation $\omega_i^2 = \lambda_i$. The eigenvalue problem in Equation 13 is solved using the default SLEPc-based Krylov–Schur solver with a shift-and-invert spectral transformation for extraction of interior eigenvalues.[45,46]

The calculated frequencies of both the reference and the IGA-based model are reported in Table 2, with three levels of discretization used for the IGA-based model. Mesh 1 consists of 10 800 cubic NURBS elements and 16 367 control points over 28 NURBS surfaces. Mesh 2 is obtained by performing a single global h-refinement of Mesh 1, and Mesh 3 is obtained by performing two global h-refinements of Mesh 1. As discussed previously, the presented model and the reference model use slightly different approaches for capturing material thickness distributions. Additionally, it is likely that some minute geometrical differences exist, and it does not appear that Resor[48] uses a level of discretization that can produce fully converged solutions. Some differences in computed frequencies of vibration are therefore expected. As Table 2 shows, however, the first six computed frequencies all agree reasonably well, with a largest difference of 5.63%, or approximately 0.05 Hz, and a lowest difference of 0.61%. Thus, the IGA-based model is considered valid.

TABLE 2 Frequencies of vibration of the reference model and the IGA-based model for three different levels of discretization. Mesh 1 indicates the coarsest discretization and Mesh 3 indicates the finest. Blade modes, v_i, depicted at right for Mesh 1.

		Mesh 1		Mesh 2		Mesh 3	
	Ref[48]	Freq (Hz)	Diff (%)	Freq (Hz)	Diff (%)	Freq (Hz)	Diff (%)
1st flapwise[a]	0.87	0.919	5.63	0.919	5.63	0.919	5.63
1st edgewise[b]	1.06	1.054	0.57	1.054	0.57	1.053	0.66
2nd flapwise[c]	2.68	2.809	4.81	2.808	4.78	2.808	4.78
2nd edgewise[d]	3.91	3.886	0.61	3.884	0.66	3.883	0.69
3rd flapwise[e]	5.57	5.666	1.72	5.660	1.62	5.658	1.58
1st torsion[f]	6.45	6.698	3.84	6.694	3.78	6.692	3.75

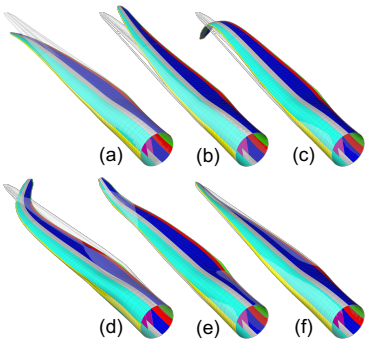

3.3 | Buckling analysis

As discussed in Section 1, computing buckling load factors is one of the key applications of high-fidelity structural analysis methods in blade design. Linear buckling analysis, or eigenvalue buckling analysis, entails solving the equation

$$\left(\mathbf{K}^{\text{lin}} + \lambda_i \mathbf{K}_g\right) v_i = 0\,, \tag{14}$$

where $\mathbf{K}^{\text{lin}}$ is the linear stiffness matrix of the structure, $\mathbf{K}_g$ is the geometric stiffness matrix, and λ_i is the i^{th} eigenvalue associated with mode vector v_i. In this context, an eigenvalue λ_i is a scalar multiplier of the applied loads that will, in theory, cause buckling of the structure. The PETSc-based `SuperLU_DIST`[50] direct solver is employed to solve the initial linear problem posed by Equation 10 prior to constructing $\mathbf{K}_g$. The eigenvalue problem posed in Equation 14 is addressed by again employing the default SLEPc-based Krylov–Schur solver with a shift-and-invert spectral transformation.[45,46]

Comparison of IGA buckling results to the reference[48] is complicated by the fact that buckling analysis is load-dependent. Load distributions are not provided by Resor[48]; hence, aeroelastic simulations, from which distributed loads can be extracted, are performed. This process will be described in greater detail in Section 4.1. For the purposes of simple comparison, the extreme 50-year wind load case with 15 degrees of yaw error is simulated and the aerodynamic loads associated with the time at which the flapwise root bending moment is greatest are applied. Within the IGA-based framework, a buckling factor of 1.61 is calculated. This factor is within 2% of the lowest buckling factor of 1.64 reported by Resor for the same load case.[48]

3.4 | Mesh refinement study

The mesh refinement study using linear vibration analysis was already presented in Section 13 and Table 2. However, Resor[48] performs a mesh refinement study via linear buckling analysis. Thus, in this section, a similar, IGA-based mesh refinement study is performed for comparison.

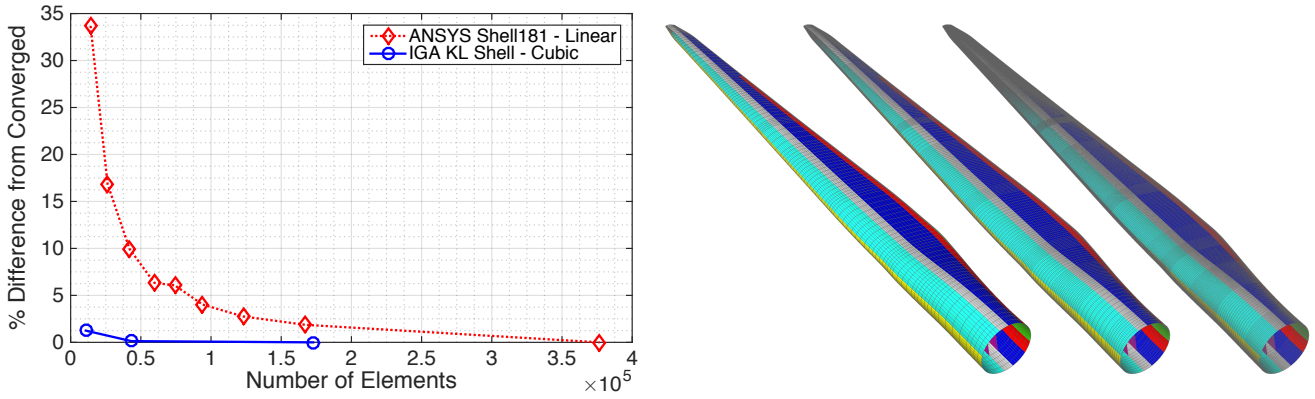

FIGURE 5 Convergence of lowest predicted buckling load multiplier under mesh refinement relative to the most converged solution for both IGA computations (blue) and computations performed by Resor[48] (red). Mesh densities for IGA Meshes 1, 2, and 3 shown at right.

Resor[48] performs such a study for flapwise buckling of the NREL/SNL 5 MW blade modeled using four-noded ANSYS Shell181 thick-shell elements, the results of which are reproduced in Figure 5. Resor[48] records the maximum bending moment that occurs at each station throughout numerous load cases, and then, in buckling analysis, applies a load distribution to recreate this maximum bending moment distribution. While this is an ideal approach, it requires significant additional processing of time histories, loads, and applied forces. Thus, for this study, the loads corresponding to largest flapwise root bending moment are employed and it is assumed that the use of somewhat different loading scenarios for the reference blade and the presented blade has a negligible effect. According to both the analyses performed by Resor[48] and analyses performed for this work, the largest bending moment occurs during the extreme 50-year wind with a parked rotor and 15 degrees of yaw misalignment. In the IGA framework, these loads are distributed to all blade surfaces evenly in the chordwise direction and varying in the spanwise direction according to the load profile produced by aeroelastic analysis. Resor[48] performs mesh refinement by incrementally reducing the target element size used in a meshing algorithm, whereas refinement in the IGA framework is performed via h-refinement. The three IGA meshes used in this study correspond to Meshes 1, 2, and 3 in Table 3.2.

Figure 5 shows the results of the two mesh refinement studies. The resultant buckling loads are normalized with respect to the most refined solution. It should be noted that the results in Figure 5 do not constitute a one-to-one comparison of traditional FEA to IGA. The element type employed by Resor[48], ANSYS Shell181, is a four-node, thick-shell, linear element with six degrees of freedom at each node, whereas the NURBS-based model employs cubic NURBS with three degrees of freedom at each node and a thin-shell formulation. The total number of degrees of freedom (DOF) used in an analysis is significant because it indicates the size of the linear algebra problem that must be solved; smaller problems can typically be solved more quickly. Resor[48] only provides the number of elements used in the reference analysis, and the number of elements and DOF cannot be directly related without any knowledge of the mesh topology. Still, the relative number of elements is at least indicative of the relative number of DOF, especially for meshes with fairly uniform discretization.

The results in Figure 5 demonstrate the efficiency of the presented IGA approach relative to a more traditional FEA approach. For the coarsest ANSYS-based case having approximately 14 200 elements, an error approximately 34% is observed. In sharp contrast, when using 10 800 elements in the IGA framework an error of only 1.25% is observed, a level of error that is not achieved even by using more than 160 000 ANSYS Shell181 elements. Additionally, moderate refinement quickly drives error towards zero for isogeometric analysis.

4 | DESIGN OPTIMIZATION

The great efficiency of the IGA-based framework for wind turbine blade analysis underscores its unique applicability in the context of iterative analysis. Not only can the use of IGA provide time savings, but it can also provide benefits in regards to other practical issues such as mesh generation, data transfer, and data storage. Thus, this section utilizes the aforementioned framework to perform IGA-buckling-constrained optimization of the blade mass and material cost of the NREL/SNL 5 MW blade.

4.1 | Aeroelastic simulation

A critical task in wind turbine blade design is quantification of the aerodynamic loads, a complicated endeavor due to the interdependence of aerodynamic and structural factors. Advanced aeroelastic codes such as FAST[51] and HAWC2[52] utilize reduced-order models to predict overall wind turbine behavior subject to the effects of aerodynamics, structural dynamics, control, and other factors. For the present optimization problem, NREL's FAST is employed in conjunction with high-fidelity IGA. Load analysis is performed using the methodology presented by Resor[48]. Resor[48] identifies a subset of IEC 61400 design load cases (DLCs) that are considered to be the most likely design drivers for a 5 MW wind turbine blade: DLCs 1.2, 1.3, 1.4, 1.5, 1.6, and 6.3.

For the purposes of comparison, the evaluation of these load cases, as outlined by Resor,[48] is reproduced as nearly as possible using FAST version 8 implemented in the style of the Framework for Unified Systems Engineering and Design of Wind Plants (FUSED-Wind),[53] an open-source framework for multidisciplinary optimization of wind energy systems developed as an extension to the NASA-developed OpenMDAO.[54] While the exact results obtained differ somewhat from those reported by Resor[48] because of slightly different material distributions, different versions of FAST, and potentially different simulation settings that are not described by Resor[48], the overall trends and conclusions corroborate the reference analysis. Neither ultimate stress analysis nor fatigue analysis are shown to be design-governing, with all stress values falling below the design limits for each material and Miner's fatigue analysis indicating a material life of well over 20 years. A maximum tip deflection of 6.34 m is observed during the ECD load case having a negative gust at rated speed (ECD-R), whereas a maximum flapwise moment of 23 130 kN is observed during the 50-year extreme wind load case with positive 15 degrees of misalignment (EWM50+15). The aerodynamic loads corresponding to this case are used to calculate the buckling load factor of 1.61 discussed in Section 3.3.

Given that the NREL/SNL 5 MW reference blade design appears to be governed by the EWM50+15 and ECD-R load cases, only these cases are utilized in the optimization problem, significantly reducing the number of aeroelastic simulations that must be performed for each design iteration. For each set of design parameters, the procedure for determining cost function value is: (1) calculate the reduced-order blade beam properties using NREL's PreComp,[55] (2) use FAST to perform aeroelastic analysis of the EWM50+15 and ECD-R load cases and calculate maximum stresses and tip deflection, (3) extract instantaneous aerodynamic loads corresponding to the maximum root bending moment in both the flapwise and edgewise directions, (4) perform two independent IGA-based buckling analyses using the loads extracted in the previous step, and (5) calculate the value of the cost function using constraints, calculated via FAST and IGA, and blade mass and material cost values calculated within the IGA-based buckling analysis.

4.2 | Objective function

The ultimate goal throughout the design of any wind turbine component is to reduce the overall cost of energy. Quantifying the effect of design changes at the component level on the overall cost of energy, however, is a nontrivial task that requires considerable systems-level design and analysis capabilities. Thus, a simpler approach is adopted in which both blade mass and blade material cost are to be reduced. Both mass reduction and material cost reduction could have a beneficial impact on cost of energy; blade mass reduction entails reduced loads on nacelle and tower, which could lead to reduced cost overall, whereas blade material cost is more obviously a contributor to turbine capital cost.

The optimization problem is posed as follows:

$$\begin{aligned} &\text{minimize} && f(\mathbf{x}) \\ &\text{subject to} && c_i(\mathbf{x}) \leq 0\,, \qquad i = 1, \ldots, n_c\,, \\ & && \mathbf{x} \in \boldsymbol{\Omega}\,, \end{aligned} \tag{15}$$

where $\mathbf{x}$ are the design variables; $f(\mathbf{x})$ is the objective function; $c_i(\mathbf{x})$ are the n_c inequality constraints, and $\boldsymbol{\Omega}$ are the acceptable ranges for the design variables. The objective function, $f(\mathbf{x})$, is defined

$$f(\mathbf{x}) = w\frac{M(\mathbf{x}) - M_{ref}}{M_{ref}} + (1 - w)\frac{C(\mathbf{x}) - C_{ref}}{C_{ref}}\,, \tag{16}$$

where $M(\mathbf{x})$ is the blade mass for a given set of design variables, M_{ref} is the mass of the reference blade design, $C(\mathbf{x})$ is the total blade material cost for a given set of design variables, C_{ref} is the reference total material cost, and w is the weighting variable indicating the relative importance of mass and cost reduction, respectively. For this example, a weighting of $w = 0.5$ is used such that mass reduction and material cost reduction are valued equally. Blade mass is calculated using the various material densities given by Resor.[48] The cost of the majority of the materials is dictated by the price per kilogram reported by Griffith and Johanns,[56] summarized in Table 3. Fiberglass materials are priced as dry fibers; the fiber volume fractions and the cost of resin can be used to determine the infused cost. Alternatively, foam core is priced first on the basis of kitted area and then according to material thickness.

TABLE 3 The price of the various materials used in the NREL/SNL 5 MW blade design. Fiberglass costs (E-LT-5500, SNL Triax, and Saertex) are based on dry fiber material whereas UD Carbon material is pre-impregnated.

Material	Price ($/kg)	Kitting Cost ($/m^2)	Thickness Cost ($/mm)
Foam	-	20.00	0.50
Gelcoat	14.00	-	-
E-LT-5500	2.97	-	-
SNL Triax	2.97	-	-
Saertex	2.97	-	-
Resin	4.65	-	-
UD Carbon	26.40	-	-

4.3 | Constraints

One can restate the constrained optimization problem, Equation 15, as an unconstrained optimization problem by incorporating the constraints into the original objective function using the exterior penalty method.[57] This yields a pseudo-objective function

$$\Phi(\mathbf{x}) = w\frac{M(\mathbf{x}) - M_{ref}}{M_{ref}} + (1-w)\frac{C(\mathbf{x}) - C_{ref}}{C_{ref}} + \sum_{i=1}^{n_c} \beta_i \max(0, c_i(\mathbf{x}))^2 , \tag{17}$$

where β_i is a large penalty parameter. An unconstrained optimization problem is ultimately solved:

$$\begin{aligned} &\text{minimize} \quad \Phi(\mathbf{x}) \\ &\text{subject to} \quad \mathbf{x} \in \boldsymbol{\Omega} . \end{aligned} \tag{18}$$

This exterior penalty strategy presents a straightforward but effective way to incorporate constraints into the objective function. The strategy is also beneficial in that it greatly increases the number of optimization methods that can be used to solve the problem.

Upon simulating the EWM50+15 and ECD-R load cases in FAST, many of the constraints $c_i(\mathbf{x})$ can be directly calculated. One set of constraints is used to state that the maximum stresses in each structural material across the entirety of the blade should not exceed their maximum tensile strength with respect to a load factor:

$$c_j(\mathbf{x}) = \sigma_{max_j}(\mathbf{x}) - \frac{\sigma_{UT_j}}{\gamma_u} \leq 0 , \qquad j = 1, \ldots, n_m , \tag{19}$$

where σ_{max_j} is the maximum stress experienced by each material, σ_{UT_j} is the ultimate tensile strength of the material, n_m is the number of materials for which failure is a design concern, and γ_u is the safety factor used for evaluation of ultimate strength. For this work, $\gamma_u = 1.755$.[48] Stresses are calculated using the approach described by Resor.[48]

A tower clearance constraint can be similarly defined:

$$c_{n_m+1}(\mathbf{x}) = \delta_{tip}(\mathbf{x}) - \frac{\delta_{avail}}{\gamma_t} \leq 0 , \tag{20}$$

where δ_{tip} is the maximum out-of-plane displacement experienced by any of the blades throughout all simulations, δ_{avail} is the available tower clearance, and γ_t is the safety factor used for tip clearance evaluation. Here, $\delta_{avail} = 10.50$ m and $\gamma_t = 1.485$.[48]

Lastly, after extracting the aerodynamic loads that produce the maximum bending moment in both the flapwise and edgewise directions, IGA-based linear buckling analysis can be performed. The corresponding constraint is given as

$$c_{n_m+2}(\mathbf{x}) = \gamma_b - \min(\lambda_{flap}(\mathbf{x}), \lambda_{edge}(\mathbf{x})) \leq 0 , \tag{21}$$

where λ_{flap} is the lowest buckling load factor as a result of the loads corresponding to the maximum flapwise bending moment, λ_{edge} is the lowest buckling load factor as a result of the loads corresponding to the maximum edgewise bending moment, and γ_b is the factor of safety used for linear buckling evaluation; in this case, $\gamma_b = 1.62$.[48]

4.4 | Design variables

The selection of design variables is governed by both practical constraints and the design objectives. For this problem, a relatively flexible design space is created within which the thickness of many of the material stacks can be varied at different regions over the blade span. Some stack definitions remain invariant, such as the external gelcoat, which does not play an important role in blade structure and which would not be modified

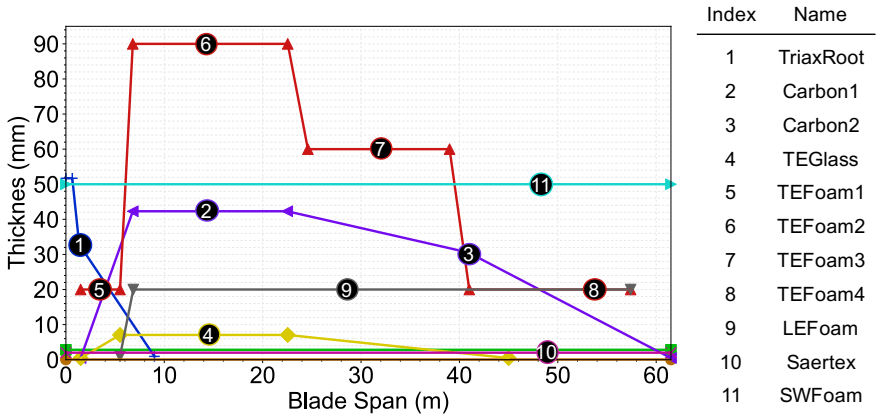

FIGURE 6 Material stack thickness distributions with design variables identified by numerical markers. For variables with markers on horizontal line segments, thickness variation is applied to the line segment end points. For variables with markers directly on points, thickness variation is applied directly to the point. Indices of the variables Δt_i and corresponding names given at right.

for structural purposes, and the triax skins, which are thin layers of fiberglass used consistently throughout the blade structure to maintain general structural integrity. Additionally, the thickness of the fiberglass at the root is not modified as it is assumed that the reference thickness is defined to account for the installation of bolts.

Figure 6 identifies the $n_v = 11$ design variables that are selected. Each variable of index i is associated with either one or two of the thickness distribution definition points illustrated in Figure 6. For variables indicated by markers in the middle of a line segment, the thickness of the two associated end points is modified by a common variable Δt_i. For variables indicated by markers directly overlapping a point, the thickness at that single point is modified by a variable Δt_i. This is illustrated by the expression

$$t_i = t_{ref} + \Delta t_i\,, \qquad i = 1, \ldots, n_v\,, \tag{22}$$

where t_i denotes the thickness at the point or points associated with design variable i for a given optimization iteration, t_{ref} denotes the reference thickness of the corresponding point or points, and Δt_i denotes the value of the design variable for a given optimization iteration.

4.5 | Implementation and solution strategies

The optimization problem represented by Equation 18 is implemented in OpenMDAO,[54] a python-based software for multidisciplinary design analysis and optimization. FAST-based aeroelastic analyses are performed through the OpenMDAO-based FUSED-Wind[53]; thus, the analyses can be performed in parallel. A similar module is developed to dispatch the two IGA-based buckling analyses in serial from within OpenMDAO. Using this setup, each function evaluation takes approximately 12 minutes on two cores of a Linux machine with Intel Xeon E5-2699 v3 2.30 GHz processors. Each optimization problem is solved using two cores, with clear possibilities for improved efficiency and parallelism in the future. OpenMDAO provides a variety of optimization methods as well as the ability to automatically calculate finite-difference-based gradients. The pyOpt-based[58] Sequential Least Squares Programming (SLSQP) method is selected for its relative robustness and ability to incorporate gradient information. A penalty coefficient of $\beta_i = 1000$ is used for all constraints.

Experience indicates that the solution space of this particular optimization problem is quite complicated, with a large number of local minima. Because the SLSQP method features no mechanisms for escaping regions of local minima and because a more thorough exploration of the design space is desired, multiple optimizations are performed with different starting points. Specifically, Latin hypercube sampling, which has been shown to be more effective than purely random sampling,[59] is used to generate 15 distinct starting points for the 11 design variables.

4.6 | Results and discussion

The initial mass and material cost of each sample point as well as associated optimized mass and material cost are plotted in Figure 7. The average number of function evaluations for each optimization is approximately 424. The wide variety of optimized designs that are generated confirm that the function space has many local minima, some of which do not perform well from a blade mass and material cost perspective, and underscores the

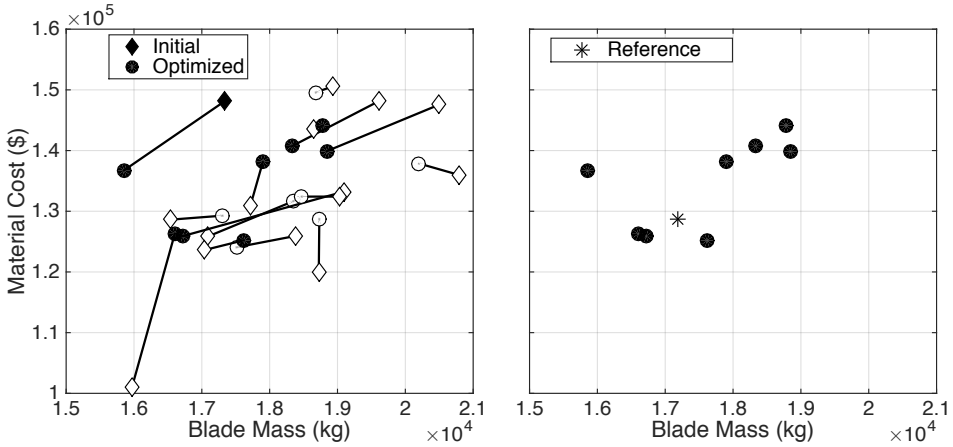

FIGURE 7 At left, blade mass and material cost of each starting point (diamonds) and blade mass and material cost of corresponding optimized designs (circles). Unfilled points signify invalid designs as indicated by an objective function penalization of greater than 0.05. At right, blade mass and material cost of only valid optimized points and reference design.[48]

TABLE 4 Optimization and relative performance details of two of the best-performing optimized designs.

Result Name	Initial Objective	Final Objective	Relative Mass (%)	Relative Cost (%)	Function Evaluations
Balanced	1086.29	-0.026	**-3.39**	**-1.80**	498
Lightweight	0.08	-0.007	**-7.74**	**+6.32**	266

value of utilizing many starting points. In general, however, one can see that, in the majority of the problems, either mass is decreased, material cost is decreased, the level of constraint violation is decreased, or some combination of these pseudo-objective reduction mechanisms is achieved.

Detailed results of two of the optimizations are given in Table 4 and the values of the corresponding design variables are shown in Figure 8. The two designs in Table 4 are among the best-performing optimized designs, and both of them, according to the objective function, Equation 17, perform better than the baseline 5 MW blade design. However, performance improvement is achieved differently in each of these two designs. In the design designated here as the "Balanced" design, both blade mass and material cost are reduced, demonstrating that it is possible to achieve improvement of both blade mass and material cost metrics simultaneously. This balanced design technically performs the best from the perspective of Equation 17. The "Lightweight" design, however, demonstrates improvement only of the blade mass metric, with an accompanying material cost increase. While material cost increase is not desirable from the perspective of the objective function, the drastic blade mass reduction of 7.74 % could enable even more cost reduction in downstream components such as the drivetrain or the tower. Such interactions are notoriously difficult to accurately capture on the systems level. Thus, different optimized designs may be preferable for different turbine platforms or to satisfy unique design goals.

Distinct performance metrics are fundamentally achieved by the different material distributions generated by the design variable values in Figure 8. The left side of Figure 9 shows, for the baseline, balanced, and lightweight 5 MW designs, the total mass of the three primary types of materials: fiberglass, which includes E-LT-5500, SNL triax, Saertex, and resin; foam; and uni-directional carbon fiber. Similarly, the right side of Figure 9 quantifies the contribution of each type of material towards overall material cost in each of the three designs. For the balanced design, the mass of all three types of materials is reduced relative to the baseline design. In this case, buckling resistance is improved by more optimally distributing fiberglass and foam, as shown in Figure 8. Because the amount of each type of material is reduced in the balanced design, the overall material cost is also reduced.

The lightweight design demonstrates a substantially different approach. In the lightweight design, the amount of carbon is increased, enabling reductions in the amounts of both fiberglass and foam that are used. Carbon's high strength-to-weight ratio dictates that this exchange is quite beneficial in terms of blade mass, enabling a 7.74% mass reduction, or over 1300 kg. Due to the high cost of carbon, however, the overall material cost is adversely affected, even despite cost reduction stemming from reduced fiberglass mass. Interestingly, the total cost of foam experiences little variation from case to case despite non-zero variables associated with foam thickness. This is because the overall cost that is attributed to foam is dominated by kitting cost, determined by the total area over which the foam is applied, which is invariant in this optimization problem.

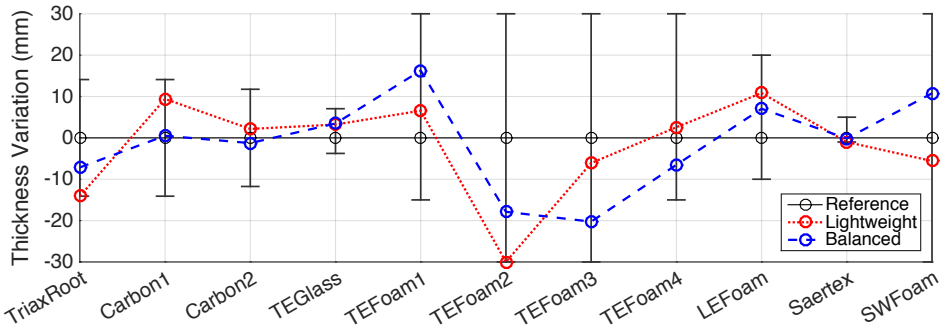

FIGURE 8 Thickness variation design variable values for the reference, balanced, and lightweight 5 MW blade designs. Bars indicate the allowable range for each design variable.

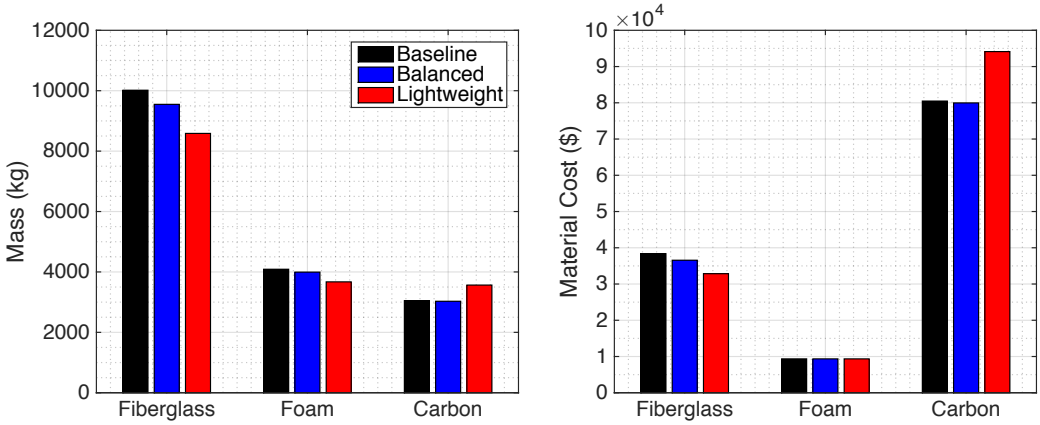

FIGURE 9 The total mass and material cost contributions of three primary types of materials—fiberglass, which includes E-LT-5500, SNL triax, Saertex, and resin; foam; and carbon—to the baseline, balanced, and lightweight 5 MW blade designs.

TABLE 5 Various performance metrics of the reference and optimized 5 MW blade designs.

Design Name	Mass (kg)	Material Cost ($)	Buckling % of SF	% Max Deflection	% σ_{UT}
Reference	17 184	128 618	100.41	90.71	37.50
Balanced	16 602	126 300	100.02	92.06	37.10
Lightweight	15 853	136 745	100.01	81.73	47.69

The results also illustrate the value of incorporating high-fidelity, IGA-based bucking analysis into such an optimization problem. Table 5 shows additional performance details of the reference, balanced, and lightweight designs, including absolute mass, absolute material cost, and relevant constraint values. The buckling load factor for both of the optimized designs is approximately 100% of the design buckling safety factor of 1.62, indicating that the buckling constraint is active. In other words, the 5 MW blade design is governed primarily by buckling in all configurations presented here. If optimization were to be performed without considering this high-fidelity analysis feedback, it is likely that this behavior would not be adequately captured, potentially increasing the workload in later design stages. Each of the two optimizations discussed here took approximately 2.5 days, a reasonable time given the modest computational power utilized.

The first buckling mode for each of the reference, balanced, and lightweight blade designs is shown in Figure 10. In the reference design, buckling occurs in the spar cap at approximately midspan. This result is reasonably consistent with the reference.[48, Table 29] In the balanced design, the first buckling mode remains concentrated in the spar cap but is shifted outboard, presumably due to the slightly reduced thickness of carbon fiber beyond 22.5 m as a result of a negative “Carbon2" variation as shown in Figure 8. Conversely, the lightweight design shows considerably different buckling

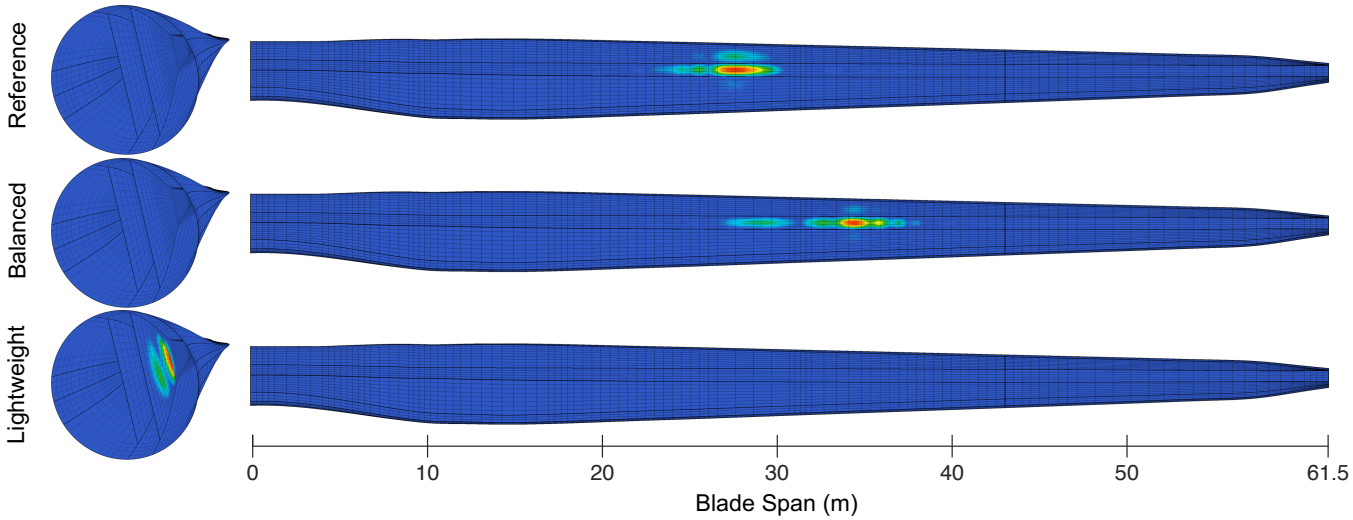

FIGURE 10 The first buckling mode of the reference (top), balanced (middle), and lightweight (bottom) 5 MW blade designs. Modes are shown in the internal structure of the blade (left) and on the suction side of the blade (right).

behavior, with the first buckling mode concentrated on the inboard region of the shear web nearest to the trailing edge. This is reasonable behavior given the increased thickness of carbon fiber in the spar cap and reduced thickness of both foam and Saertex fiberglass in the shear web.

5 | CONCLUSION

A framework is presented through which IGA-based structural analysis of wind turbine blades can be easily performed. The framework employs the efficient IGA Kirchhoff–Love shell formulation for composites and a penalty energy coupling technique to accommodate multi-patch geometry construction. The technique is capable of coupling shell interfaces with non-matching control points and discretization, eliminating the restrictive requirements imposed on the geometry construction by other methods.

For the purposes of demonstration, the NREL/SNL 5 MW blade is modeled within Rhinoceros 3D, a NURBS-based CAD modeling software. Analysis-suitable geometries can be generated from a set of input parameters within the CAD software in a matter of seconds, underscoring the seamless approach enabled by IGA. Upon inspecting the behavior of buckling solutions under mesh refinement, it is clear that the IGA-based framework is capable of providing accurate solutions using significantly fewer elements relative to a traditional FEA-based approach.

The NREL/SNL 5 MW blade is also optimized within OpenMDAO [54] using both the FAST aeroelastic tool and IGA-based buckling analysis. The cost function is defined such that minimization of both blade mass and total material cost are beneficial. Variation of material thickness profiles is enabled through 11 design variables, and constraints are defined based on the IEC 61400 requirements for material ultimate stress, maximum tip deflection, and resistance to buckling. Optimization is performed on 15 initial blade designs that are generated using Latin hypercube sampling, and multiple designs of potential interest are identified. The optimized design with the absolute lowest cost function evaluation, termed the "balanced" design, features both reduced blade mass and reduced material cost relative to the reference design. Alternatively, the "lightweight" design features a significant blade mass reduction of over 7% achieved through the employment of more carbon fiber in the spar cap. In both of these optimizations, the blade's buckling behavior governs the design, highlighting the value of incorporating high-fidelity structural analysis into blade optimization procedures.

These studies have also generated some peripheral insights. For example, as initial experience suggested and as Figure 7 confirms, the objective function space defined for this problem is non-smooth, with numerous local minima. Because both blade mass and material cost have simple, smooth relationships to the design variables, the overall pseudo-objective function complexity appears to stem from the constraints, in particular the design-governing buckling behavior. It would be reasonable to expect this behavior for other similarly-defined optimization problems. Of course, the optimization procedure presented here is limited in scope. If buckling analysis were performed for loads applied over a wider range of load angles, for example, it is quite possible that the results would differ. Still, this work provides a framework to perform such explorations more easily, more efficiently, and more accurately. It also provides some optimized design alternatives which perform better than the reference design, potentially providing a starting point for future design studies.

ACKNOWLEDGMENTS

A.J. Herrema was supported by the U.S. National Science Foundation (NSF) Grant No. DGE-1069283 which funds the activities of the Integrative Graduate Education and Research Traineeship (IGERT) in Wind Energy Science, Engineering, and Policy (WESEP) at Iowa State University. J. Kiendl was partially supported by the Onsager fellowship program of the Norwegian University of Science and Technology. The authors would like to thank Dr. Baskar Ganapathysubramanian at Iowa State University for suggestions regarding the optimization performed in this work; Dr. Frederik Zahle and Dr. Michael McWilliam, both at Denmark Technical University, for helpful discussions regarding OpenMDAO and multidisciplinary blade design; and Dr. Katherine Dykes at NREL for support and guidance in developing a programmatic wrapper for FAST.

References

1. Manwell JF, McGowan JG, Rogers AL. *Wind Energy Explained: Theory, Design and Application, 2nd ed.* Chichester: John Wiley & Sons; 2009.
2. Money C, Hand M, Bolinger M, Rand J, Heimiller D, Ho J. *2015 Cost of Wind Energy Review.* NREL/TP-6A20-66861: National Renewable Energy Laboratory. Golden, CO; 2017.
3. Cox K, Echtermeyer A. Effects of composite fiber orientation on wind turbine blade buckling resistance. *Wind Energy.* 2014;17(12):1925–1943.
4. Cox K, Echtermeyer A. Structural design and analysis of a 10MW wind turbine blade. *Energy Procedia.* 2012;24:194–201.
5. Chen X, Zhao X, Xu J. Revisiting the structural collapse of a 52.3 m composite wind turbine blade in a full-scale bending test. *Wind Energy.* 2017;17:657–669.
6. Lindgaard E, Lund E. Nonlinear buckling optimization of composite structures. *Computer Methods in Applied Mechanics and Engineering.* 2010;199(37–40):2319–2330.
7. Jensen FM, Weaver PM, Cecchini LS, Stant H, Nielsen RF. The Brazier effect in wind turbine blades and its influence on design. *Wind Energy.* 2012;15(2):319–333.
8. Chehouri A, Younes R, Ilinca A, Perron J. Review of performance optimization techniques applied to wind turbine blades. *Applied Energy.* 2015;142:361–388.
9. Xudong W, Zhu WJ, Sørensen JN, Jin C. Shape optimization of wind turbine blades. *Wind Energy.* 2009;12(8):781–803.
10. Fuglsang P, Madsen HA. Optimization method for wind turbine rotors. *Journal of Wind Engineering and Industrial Aerodynamics.* 1999;80(1–2):191–206.
11. Lanzafame R, Messina M. Fluid dynamics wind turbine design: Critical analysis, optimization and application of BEM theory. *Renewable Energy.* 2007;32(14):2291–2305.
12. Benini E, Toffolo A. Optimal design of horizontal-axis wind turbines using blade-element theory and evolutionary computation. *Journal of Solar Energy Engineering.* 2002;124:357–363.
13. Campobasso MS, Minisci E, Caboni M. Aerodynamic design optimization of wind turbine rotors under geometric uncertainty. *Wind Energy.* 2014;19(1):51–65.
14. Fuglsang P, Bak C, Schepers JG, et al. Site-specific design optimization of wind turbines. *Wind Energy.* 2002;5:261–279.
15. *Wind turbines–Part 1: Design requirements.* IEC 61400-1: International Electrotechnical Commission. Geneva, Switzerland; 2005.
16. Hughes TJR, Cottrell JA, Bazilevs Y. Isogeometric analysis: CAD, finite elements, NURBS, exact geometry and mesh refinement. *Computer Methods in Applied Mechanics and Engineering.* 2005;194:4135–4195.
17. Benson DJ, Bazilevs Y, Hsu M-C, Hughes TJR. A large deformation, rotation-free, isogeometric shell. *Computer Methods in Applied Mechanics and Engineering.* 2011;200:1367–1378.
18. Morganti S, Auricchio F, Benson DJ, et al. Patient-specific isogeometric structural analysis of aortic valve closure. *Computer Methods in Applied Mechanics and Engineering.* 2015;284:508–520.
19. Bazilevs Y, Hsu M-C, Akkerman I, et al. 3D simulation of wind turbine rotors at full scale. Part I: Geometry modeling and aerodynamics. *International Journal for Numerical Methods in Fluids.* 2011;65:207–235.
20. Bazilevs Y, Hsu M-C, Kiendl J, Wüchner R, Bletzinger K-U. 3D simulation of wind turbine rotors at full scale. Part II: Fluid–structure interaction modeling with composite blades. *International Journal for Numerical Methods in Fluids.* 2011;65:236–253.
21. Hsu M-C, Akkerman I, Bazilevs Y. High-performance computing of wind turbine aerodynamics using isogeometric analysis. *Computers & Fluids.* 2011;49:93–100.

22. Bazilevs Y, Hsu M-C, Scott MA. Isogeometric fluid–structure interaction analysis with emphasis on non-matching discretizations, and with application to wind turbines. *Computer Methods in Applied Mechanics and Engineering.* 2012;249–252:28–41.
23. Hsu M-C, Bazilevs Y. Fluid–structure interaction modeling of wind turbines: simulating the full machine. *Computational Mechanics.* 2012;50:821–833.
24. Korobenko A, Hsu M-C, Akkerman I, Tippmann J, Bazilevs Y. Structural mechanics modeling and FSI simulation of wind turbines. *Mathematical Models and Methods in Applied Sciences.* 2013;23(2):249–272.
25. Bazilevs Y, Korobenko A, Deng X, Yan J. Novel structural modeling and mesh moving techniques for advanced fluid–structure interaction simulation of wind turbines. *International Journal for Numerical Methods in Engineering.* 2014;102(3-4):766–783.
26. Bazilevs Y, Deng X, Korobenko A, Scalea F, Todd MD, Taylor SG. Isogeometric fatigue damage prediction in large-scale composite structures driven by dynamic sensor data. *Journal of Applied Mechanics.* 2015;82(9):091008–12.
27. Hsu M-C, Wang C, Herrema AJ, Schillinger D, Ghoshal A, Bazilevs Y. An interactive geometry modeling and parametric design platform for isogeometric analysis. *Computers and Mathematics with Applications.* 2015;70:1481–1500.
28. Yan J, Korobenko A, Deng X, Bazilevs Y. Computational free-surface fluid–structure interaction with application to floating offshore wind turbines. *Computers & Fluids.* 2016;141:155–174.
29. Herrema AJ, Wiese NM, Darling CN, Ganapathysubramanian B, Krishnamurthy A, Hsu M-C. A framework for parametric design optimization using isogeometric analysis. *Computer Methods in Applied Mechanics and Engineering.* 2016;316:944–965.
30. Ferede E, Abdalla MM, Bussel GJW. Isogeometric based framework for aeroelastic wind turbine blade analysis. *Wind Energy.* 2017;20(2):193–210.
31. Bazilevs Y, Calo VM, Cottrell JA, et al. Isogeometric analysis using T-splines. *Computer Methods in Applied Mechanics and Engineering.* 2010;199:229–263.
32. Piegl L, Tiller W. *The NURBS Book (Monographs in Visual Communication), 2nd ed.* New York: Springer-Verlag; 1997.
33. Kiendl J, Bletzinger K-U, Linhard J, Wüchner R. Isogeometric shell analysis with Kirchhoff–Love elements. *Computer Methods in Applied Mechanics and Engineering.* 2009;198:3902–3914.
34. Reddy JN. *Mechanics of Laminated Composite Plates and Shells: Theory and Analysis, 2nd ed.* Boca Raton, FL: CRC Press; 2004.
35. Guo Y, Ruess M. Nitsche's method for a coupling of isogeometric thin shells and blended shell structures. *Computer Methods in Applied Mechanics and Engineering.* 2015;284:881–905.
36. Nguyen-Thanh N, Zhou K, Zhuang X, et al. Isogeometric analysis of large-deformation thin shells using RHT-splines for multiple-patch coupling. *Computer Methods in Applied Mechanics and Engineering.* 2017;316:1157–1178.
37. Ruess M, Schillinger D, Bazilevs Y, Varduhn V, Rank E. Weakly enforced essential boundary conditions for NURBS-embedded and trimmed NURBS geometries on the basis of the finite cell method. *International Journal for Numerical Methods in Engineering.* 2013;95:811–846.
38. Ruess M, Schillinger D, Özcan AI, Rank E. Weak coupling for isogeometric analysis of non-matching and trimmed multi-patch geometries. *Computer Methods in Applied Mechanics and Engineering.* 2014;269:46–731.
39. Breitenberger M., Apostolatos A., Philipp B., Wüchner R., Bletzinger K.-U.. Analysis in computer aided design: Nonlinear isogeometric B-Rep analysis of shell structures. *Computer Methods in Applied Mechanics and Engineering.* 2015;284:401–457.
40. Dornisch W, Vitucci G, Klinkel S. The weak substitution method - an application of the mortar method for patch coupling in NURBS-based isogeometric analysis. *International Journal for Numerical Methods in Engineering.* 2015;103(3):205–234.
41. Duong TX, Roohbakhshan F, Sauer RA. A new rotation-free isogeometric thin shell formulation and a corresponding continuity constraint for patch boundaries. *Computer Methods in Applied Mechanics and Engineering.* 2017;316:43–83.
42. Kiendl J, Bazilevs Y, Hsu M-C, Wüchner R, Bletzinger K-U. The bending strip method for isogeometric analysis of Kirchhoff–Love shell structures comprised of multiple patches. *Computer Methods in Applied Mechanics and Engineering.* 2010;199:2403–2416.
43. Balay S, Abhyankar S, Adams MF, et al. *PETSc Users Manual.* ANL-95/11 - Revision 3.7: Argonne National Laboratory. Lemont, IL; 2016.
44. Balay S, Gropp WD, McInnes LC, Smith BF. Efficient management of parallelism in object oriented numerical software libraries. In: Arge E, Bruaset AM, Langtangen HP, eds. *Modern Software Tools in Scientific Computing*, 163–202. Birkhäuser Press; 1997.
45. Hernandez V, Roman JE, Vidal V. SLEPc: A Scalable and Flexible Toolkit for the Solution of Eigenvalue Problems. *ACM Trans. Math. Software.* 2005;31(3):351–362.
46. Roman JE, Campos C, Romero E, Tomas A. *SLEPc Users Manual.* DSIC-II/24/02 - Revision 3.7: D. Sistemes Informàtics i Computació, Universitat Politècnica de València. Valencia, Spain; 2016.

47. Jonkman J, Butterfield S, Musial W, Scott G. *Definition of a 5-MW reference wind turbine for offshore system development*. Technical Report NREL/TP-500-38060: National Renewable Energy Laboratory. Golden, CO; 2009.
48. Resor BR. *Definition of a 5MW/61.5m wind turbine blade reference model*. Technical Report SAND2013-2569: Sandia National Laboratories. Albuquerque, NM; 2013.
49. Griffith T, Ashwill TD. *The Sandia 100-meter all-glass baseline wind turbine blade: SNL100-00*. Technical Report SAND2011-3779: Sandia National Laboratories. Albuquerque, New Mexico; 2011.
50. Li XS, Demmel JW. SuperLU_DIST: A scalable distributed-memory sparse direct solver for unsymmetric linear systems. *ACM Trans. Mathematical Software*. 2003;29(2):110-140.
51. Jonkman J. *FAST*. National Renewable Energy Laboratory. https://nwtc.nrel.gov/FAST; 2015.
52. Larsen TJ. *How 2 HAWC2, the User's Manual*. Risø National Laboratory for Sustainable Energy, Technical University of Denmark. http://orbit.dtu.dk/files/7703110/ris_r_1597.pdf; 2007.
53. Réthoréx P-E, Zahle F. *Framework for Unified Systems Engineering and Design of Wind Plants (FUSED-Wind)*. National Renewable Energy Laboratory, Technical University of Denmark. http://www.fusedwind.org/; 2017.
54. Gray J, Moore KT, Naylor BA. *OpenMDAO: An open source framework for multidisciplinary analysis and optimization*. 13th AIAA/ISSMO Multidisciplinary Analysis Optimization Conference. https://arc.aiaa.org/doi/abs/10.2514/6.2010-9101; 2010.
55. Bir G, Damiani R. *PreComp*. National Renewable Energy Laboratory. https://nwtc.nrel.gov/PreComp; 2014.
56. Griffith T, Johanns W. *Large blade manufacturing cost studies using the Sandia blade manufacturing cost tool and Sandia 100-meter blades*. Technical Report SAND2013-2734: Sandia National Laboratories. Albuquerque, NM; 2013.
57. Fletcher R. *Practical Methods of Optimization, 2nd ed*. Chichester: John Wiley & Sons; 1987.
58. Perez RE, Jansen PW, Martins JRRA. pyOpt: A Python-based object-oriented framework for nonlinear constrained optimization. *Structures and Multidisciplinary Optimization*. 2012;45(1):101–118.
59. McKay MD, Beckman RJ, Conover WJ. A comparison of three methods for selecting values of input variables in the analysis of output from a computer code. *Technometrics*. 2000;42:55–61.

How to cite this article: Herrema AJ, Kiendl J, Hsu M-C. A framework for isogeometric-analysis-based design and optimization of wind turbine blade structures. *Wind Energy*. 2018; in review.

APPENDIX

TABLE A1 Definition of cross-sectional parameters used to construct the NREL/SNL 5 MW blade model. "DP" stands for "division point."

Blade span (m)	Airfoil	TE Type	Twist (deg)	Chord (m)	Pitch Axis	DP1	DP2	DP3	DP4	DP5
0.00	circle	round	13.31	3.386	0.5	0.0295	0.4114	0.5886	0.8523	0.9705
0.30 †	circle	round	13.31	3.386	0.5	0.0294	0.4114	0.5886	0.8532	0.9706
0.40 †	interp	round	13.31	3.386	0.5	0.0293	0.4114	0.5886	0.8535	0.9707
0.50 †	interp	round	13.31	3.386	0.5	0.0293	0.4114	0.5886	0.8547	0.9707
0.60 †	interp	round	13.31	3.386	0.5	0.0292	0.4114	0.5886	0.8540	0.9708
0.70 †	interp	round	13.31	3.386	0.5	0.0291	0.4114	0.5886	0.8543	0.9709
0.80 †	interp	round	13.31	3.386	0.5	0.0291	0.4114	0.5886	0.8546	0.9709
1.37	circle	round	13.31	3.386	0.5	0.0288	**0.4114**	**0.5886**	0.8562	0.9712
1.50 †	interp	round	13.31	3.387	0.4985	0.0287	**0.4102**	**0.5868**	0.8565	0.9713
1.60 †	interp	round	13.31	3.388	0.4974	0.0286	**0.4094**	**0.5854**	0.8568	0.9714
4.10	interp*	round	13.31	3.629	0.4692	0.0272	**0.3876**	**0.5508**	0.8638	0.9728
5.50	interp	round	13.31	3.873	0.4535	0.0265	**0.3755**	**0.5315**	0.8677	0.9735
6.83	interp*	flat	13.31	4.124	0.4385	0.0257	**0.3639**	**0.5131**	0.8715	0.9743
9.00	interp	flat	13.31	4.461	0.4141	0.0245	**0.3450**	**0.4831**	0.8775	0.9755
10.25	DU99-W-405	flat	13.31	4.557	0.4	0.0238	**0.3342**	**0.4658**	0.8810	0.9762
12.00	interp	flat	12.53	4.615	0.4	0.0228	**0.3313**	**0.4687**	0.8859	0.9772
14.35	DU99-W-350	flat	11.48	4.652	0.4	0.0215	**0.3274**	**0.4726**	0.8925	0.9785
17.00	interp	flat	10.68	4.584	0.4	0.0231	**0.3230**	**0.4770**	0.8871	0.9769
18.45	interp*	flat	10.16	4.506	0.4	0.0240	**0.3206**	**0.4794**	0.8841	0.9760
20.50	interp	flat	9.63	4.374	0.4	0.0253	**0.3172**	**0.4828**	0.8800	0.9747
22.55	DU97-W-300	flat	9.01	4.249	0.4	0.0265	**0.3138**	**0.4862**	0.8758	0.9735
24.60	interp	flat	8.40	4.132	0.4	0.0278	**0.3104**	**0.4896**	0.8716	0.9722
26.65	DU91-W-250	flat	7.79	4.007	0.4	0.0291	**0.3070**	**0.4930**	0.8674	0.9709
30.75	DU91-W-250	flat	6.54	3.748	0.4	0.0316	**0.3003**	**0.4997**	0.8590	0.9684
32.00	interp	flat	6.18	3.672	0.4	0.0323	**0.2982**	**0.5018**	0.8565	0.9677
34.85	DU93-W-210	flat	5.36	3.502	0.4	0.0341	**0.2935**	**0.5065**	0.8506	0.9659
37.00	interp	flat	4.75	3.373	0.4	0.0354	**0.2899**	**0.5101**	0.8462	0.9646
38.95	DU93-W-210	flat	4.19	3.256	0.4	0.0366	**0.2867**	**0.5133**	0.8423	0.9634
41.00	interp	sharp	3.66	3.133	0.4	0.0379	**0.2833**	**0.5167**	0.8381	0.9621
42.00 †	interp	sharp	3.40	3.073	0.4	0.0385	**0.2817**	**0.5183**	0.8360	0.9615
43.04 ‡	NACA-64-618	sharp	3.13	3.010	0.4	0.0391	**0.2799**	**0.5201**	0.8339	0.9609
45.00	interp	sharp	2.74	2.893	0.4	0.0403	**0.2767**	**0.5233**	0.8339	0.9597
47.15	NACA-64-618	sharp	2.32	2.764	0.4	0.0416	**0.2731**	**0.5269**	0.8339	0.9584
51.25	NACA-64-618	sharp	1.53	2.518	0.4	0.0442	**0.2664**	**0.5336**	0.8339	0.9558
54.67	NACA-64-618	sharp	0.86	2.313	0.4	0.0463	**0.2607**	**0.5393**	0.8339	0.9537
57.40	NACA-64-618	sharp	0.37	2.086	0.4	0.0479	**0.2562**	**0.5438**	0.8339	0.9521
60.13	NACA-64-618	sharp	0.11	1.419	0.4	0.0705	**0.1886**	**0.6114**	0.8339	0.9226
61.50	NACA-64-618	sharp	0.00	1.086	0.4	0.0921	0.1236	0.6764	0.8339	0.9079

Rows highlighted in grey indicate cross sections used for aerodynamic analysis. Division points at which a shear web is defined indicated by **boldface**.
*Indicates that an airfoil definition given by Jonkman et al.[47] was replaced by an interpolated profile for the purposes of smooth geometry.[48]
†Indicates stations that are ignored during IGA model construction in order to achieve more uniform spanwise NURBS discretization.
‡Indicates the spanwise location at which the trailing edge reinforcement terminates.